Computational details

Density functional theory(DFT) calculations were performed using the projector-augmented wave(PAW) method and the local spin density approximation(LSDA) for the exchange-correlation potential, which are implemented in the Vienna Ab-initio Simulation Package(VASP).[1, 2] PAW potential with valence configurations of $5s^25p^65d^16s^2$ for La, $4s^24p^65s^2$ for Sr, $3d^74s^1$ for Fe, and $2s^22p^4$for O were used to describe the valence electrons. To consider on-site Coulomb interaction of the d orbital electrons on Fe, the LSDA+U method was performed using the Dudarev formalism with U = 5.4eV, which describes well bandgaps of $LaFeO_3$ and $SrFeO_3$.[3-5] A plane wave cut off energy of 520eV was used for the representation of the wave functions and k-point sampling of gamma-centered 8*8*8 mesh was used for Brillouin zone integration. Structures were relaxed until the Hellmann-Feynman force on each atom was below 0.01eV/Å. The obtained lattice parameters of the cubic $SrFeO_3$ system are a=7.571Å. This study assumed ferromagnetic state for the calculations due to the computational difficulty on representing paramagnetic state.[6, 7] In addition, Fe magnetic moment in $La_{0.5}Sr_{0.5}FeO_{3-\delta}$ is calculated in high spin state, corresponding to $3.98\mu_B$ for $La_{0.5}Sr_{0.5}FeO_3$, because high spin state is energetically favorable and matches well with experimental observations that $La_{0.5}Sr_{0.5}FeO_{3-\delta}$ has intermediate Fe valence charge between $SrFeO_3$ and $LaFeO_3$,[8] high spin Fe of $2.96\mu_B$ and $4.6\mu_B$, respectively.[9, 10]

In this study, we considered 6 different La/Sr arrangements (Fig. S1) and 3 different oxygen stoichiometries (δ=0, 0.125 and 0.25). As a result, a total of 18 different structures are considered to understand the effect of oxygen stoichiometry on the variation of electronic structure. At δ=0, the energy difference between the lowest (-38.66eV/f.u.) and the highest (-38.61eV/f.u.) is only 0.05 eV/f.u.. Thus, we assume that real disordered $La_{0.5}Sr_{0.5}FeO_{3-\delta}$ has a combination of 6 different arrangements and so all 6 La/Sr arrangements are considered.[6, 11] Spatial location of oxygen vacancies (δ=0.125 and 0.25, corresponding to one V_O and two V_O in our simulation cell) is determined to minimize the interaction between oxygen vacancies (V_O) and to be the most energetically favorable of all possible unique V_O configurations.

Our DFT calculation predicts that $La_{0.5}Sr_{0.5}FeO_3$ is half-metallic state, which has partially-occupied spin-up band and completely-occupied spin-down band. The introduction of V_O induces V_O states and donates excess electrons in spin-up band, while it does not noticeably affect the spin-down band (Fig. S2). Thus we focus on the spin-up band of $La_{0.5}Sr_{0.5}FeO_{3-\delta}$.

As one V_O (δ=0.125) is introduced, a V_O state appears and the unoccupied states of the hybridized band decrease by excess electrons from a V_O. With two V_O (δ=0.25), two V_O states appear and the hybridized band becomes fully-occupied. As a result, electronic structure of $La_{0.5}Sr_{0.5}FeO_{3-\delta}$ changes from half-metallic state to semiconducting state. However, there can be concerns about the finite-cell effect, weak degree of disorder in La/Sr arrangement, and inaccuracy of LSDA+U method. To identify whether those concerns affect our results or not, we calculated electronic DOS for larger supercell containing 32 f.u. (160 atoms, 4x2x2 cell), for the special quasi-random structure (SQS) containing 8 f.u. (40 atoms),[12, 13] and for HSE06 method (Fig. S3, S4, S5).[14-17] The SQS was generated using the mcsqs code in the Alloy Theoretic Automatic Toolkit (ATAT).[18] The HSE06 calculations was performed to relax electronic structure on geometries from LSDA+U. The exact exchange contribution of 25% with a screening length of 0.2 $Å^{-1}$, k-point sampling of gamma-centered 2*2*2 mesh, an energy difference of $1x10^{-4}$ eV as an energy criterion, and plane wave cut off energy of 400 eV were used. The electronic DOS for the larger supercell, the SQS, and HSE06 calculations, respectively, are similar to those obtained by 2x2x2 cubic supercell and LSDA+U method, and thus we confirmed that those concerns are not crucial to understand the effects of oxygen vacancies on electrical conductivity and our results are credible.

To verify that charge state of +2 (V**Error!**) is energetically favorable state of V_O, we calculated the formation energy of V_O with different excess electrons (Fig. S6). The defect formation energy (DFE) was calculated as

$$E_{formation} = E(\text{defective system}) - E(\text{perfect system}) + \frac{1}{2}E(O_2) + q\mu_e$$

where E(defective system) is the internal energy of defective system with a V_O and charge q, E(perfect system)is the internal energy of perfect neutral system, and $\frac{1}{2}E(O_2)$ (μ_e) is oxygen (electron) chemical potential. We calculated electronic DOS for excess electron doping without an V_O to verify that electrons released from oxygen vacancies change electronic structure from metal to semiconductor (Fig. S7).

We also calculated the effective masses of hole and electron by using parabolic fittings of valence band maximum (VBM) and conduction band minimum (CBM) along high symmetric points in reciprocal space (Table S1, S2). The relationship between effective mass and electronic band structure is

$$m^* = \hbar^2(\partial^2E(k)/\partial k^2)^{-1}$$

where m^* is the effective mass, E(k) is the band dispersion relation as a function of the wave vector k. we investigated the effective masses along 7 different directions: Γ-X, Γ-Y, Γ-Z, Γ-S, Γ-U, Γ-T, and Γ-R. Since six different cation arrangements are possible, we examined the effective masses of hole and electron along a total of 42 directions and identified the minimum effective mass for dominant hole and electron pathway.

6 different La/Sr arrangements for randomly occupation of A-site

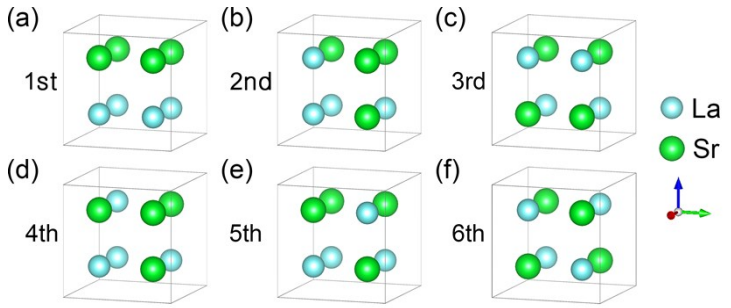

Figure. S1. 6 different La/Sr arrangements for A-site of $La_{0.5}Sr_{0.5}FeO_{3-\delta}$. Sky-blue atoms (green atoms) represent La (Sr). Fe and O are omitted for clarity. The arrangements are listed in descending order of stability, where 1st arrangement of (a) (6th arrangement of (f)) is the most stable (unstable) than others.

Since A-site of $La_{0.5}Sr_{0.5}FeO_{3-\delta}$ is randomly occupied by La or Sr with the 1:1 ratio, we identified the stable arrangement of A-site cations. Fig. S1 shows 6 different La/Sr arrangements that are possible in our simulation cell. Our calculations predict that the energy difference between 6 arrangements is minor; the energy difference between the lowest (Fig. S1(a), -38.66eV/f.u.) and the highest (Fig. S1(f), -38.61eV/f.u.) is only 0.05 eV/f.u.. Thus, we assume that real disordered $La_{0.5}Sr_{0.5}FeO_{3-\delta}$ has a combination of 6 different arrangements and so all 6 La/Sr arrangements are considered to identify the effect of oxygen vacancies on electric conductivity.

Spin-up and spin-down electronic density of states (DOS) for $La_{0.5}Sr_{0.5}FeO_{3-\delta}$ (δ=0, 0.125, and 0.25)

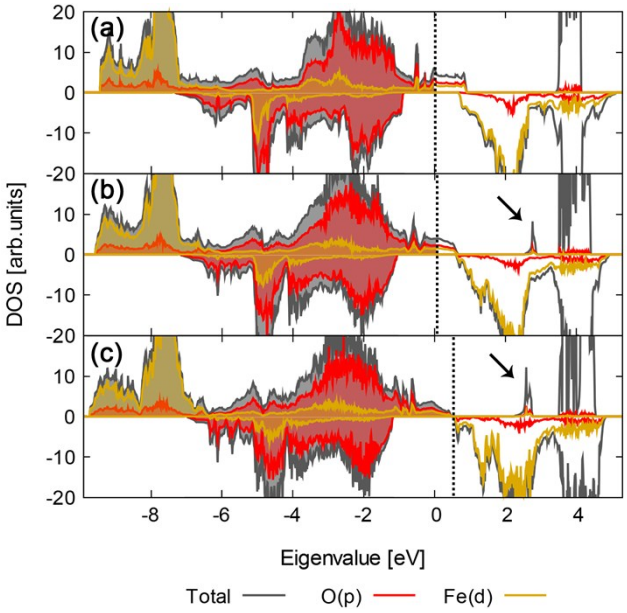

Figure. S2. Spin-up and spin-down electronic density of states (DOS) for the 2nd structure of (a) $La_{0.5}Sr_{0.5}FeO_3$, (b) $La_{0.5}Sr_{0.5}FeO_{2.875}$, and (c) $La_{0.5}Sr_{0.5}FeO_{2.750}$. DOS of positive (negative) value indicates spin-up (spin-down) band. Black lines represent total DOS and Red (gold) lines show projected DOS for O (Fe). Filled (empty) regions represent occupied (unoccupied) states. Vertical dotted lines represent valence band maximum. Black arrows indicate oxygen vacancy states.

Fig. S2(a-c) shows spin-up and spin-down DOS for $La_{0.5}Sr_{0.5}FeO_{3-\delta}$ under different oxygen deficiencies (δ=0, 0.125, and 0.25), respectively. DOS of positive value (negative value) represents spin-up (spin-down). Our projected DOS predicts that the electronic band structure of $La_{0.5}Sr_{0.5}FeO_{3-\delta}$ near Fermi level is mainly composed of hybridized band between Fe 3d-orbital and O 2p-orbital. Fig. S2(a) shows that stoichiometric $La_{0.5}Sr_{0.5}FeO_3$ is half-metallic, which has the partially filled hybridized band for spin-up and completely filled band for spin-down. As V_O are introduced, V_O states appear as shown in black arrow and the hybridized band becomes fully occupied for spin-up DOS while a remarkable change is not observed for spin-down DOS, as shown in Fig. S2(b-c). The introduction of the V_O does not affect the electronic structure of spin-down band unlike spin-up band. Thus, this study mainly focuses on the spin-up band to understand the effect of V_O on electrical conductivity.

Electronic DOS for the 4x4x2 supercell (32 f.u.) of $La_{0.5}Sr_{0.5}FeO_{3-\delta}$ (δ=0, 0.125, and 0.25)

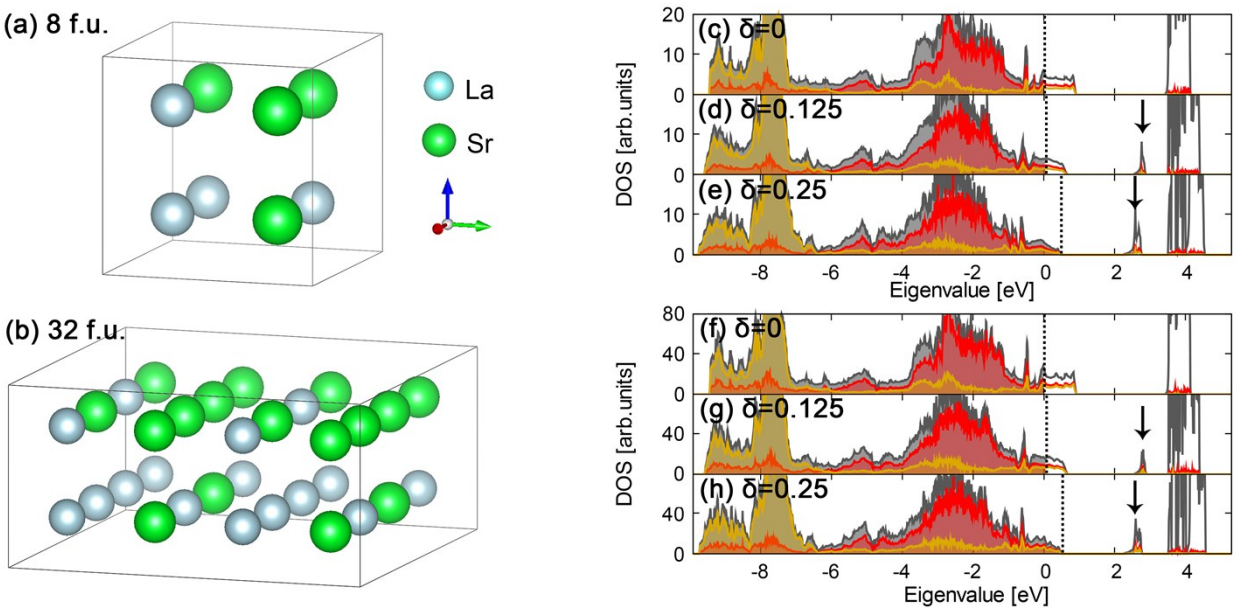

Figure. S3. DFT calculated structure for (a) the 2x2x2 cubic supercell and (b) the 4x4x2 supercell of $La_{0.5}Sr_{0.5}FeO_3$, where Fe and O are omitted for clarity. Electronic DOS for the 2x2x2 supercell of (c) $La_{0.5}Sr_{0.5}FeO_3$, (d) $La_{0.5}Sr_{0.5}FeO_{2.875}$, and (e) $La_{0.5}Sr_{0.5}FeO_{2.750}$. Electronic DOS for the 4x4x2 supercell of (f) $La_{0.5}Sr_{0.5}FeO_3$, (g) $La_{0.5}Sr_{0.5}FeO_{2.875}$, and (h) $La_{0.5}Sr_{0.5}FeO_{2.750}$. DOS of positive value indicates spin-up band. Black lines represent total DOS and Red (gold) lines show projected DOS for O (Fe). Filled (empty) regions represent occupied (unoccupied) states. Vertical dotted lines represent valence band maximum. Black arrows indicate oxygen vacancy states.

We further performed additional calculations using larger supercell to verify the energy levels of oxygen vacancies (see Fig. S3). We have observed that the energy levels of oxygen vacancies with the larger supercell (4x4x2) are still identical to those obtained with the 2x2x2 supercell. In addition, we also confirmed that the metal to semiconductor transition is observed when the oxygen vacancy concentration reaches to δ=0.25 (8 vacancies in 4x4x2 supercell). Thus, we have successfully verified that finite-size effect does not affect the energy levels of oxygen vacancies.

Electronic DOS for the SQS (8 f.u.) of $La_{0.5}Sr_{0.5}FeO_{3-\delta}$ (δ=0, 0.125, and 0.25)

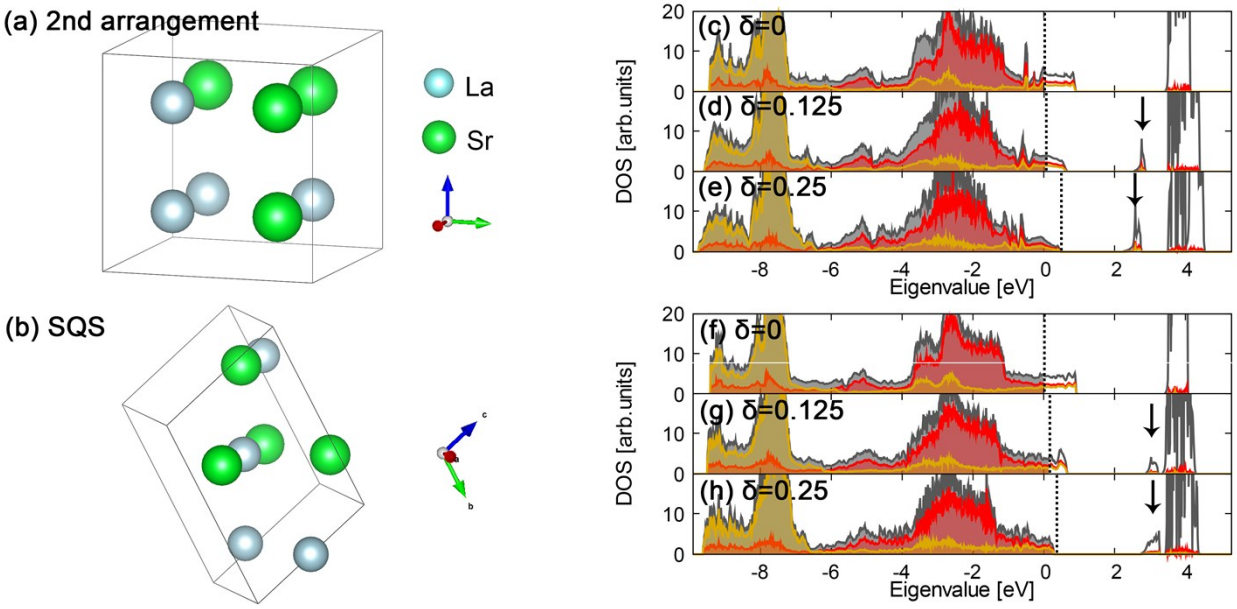

Figure. S4. DFT calculated structure for (a) the 2x2x2 cubic supercell with the 2nd La/Sr arrangement and (b) the SQS of $La_{0.5}Sr_{0.5}FeO_3$, where Fe and O are omitted for clarity. Electronic DOS for the 2x2x2 supercell of (c) $La_{0.5}Sr_{0.5}FeO_3$, (d) $La_{0.5}Sr_{0.5}FeO_{2.875}$, and (e) $La_{0.5}Sr_{0.5}FeO_{2.750}$. Electronic DOS for the SQS of (f) $La_{0.5}Sr_{0.5}FeO_3$, (g) $La_{0.5}Sr_{0.5}FeO_{2.875}$, and (h) $La_{0.5}Sr_{0.5}FeO_{2.750}$. DOS of positive value indicates spin-up band. Black lines represent total DOS and Red (gold) lines show projected DOS for O (Fe). Filled (empty) regions represent occupied (unoccupied) states. Vertical dotted lines represent valence band maximum. Black arrows indicate oxygen vacancy states.

We have performed additional calculations by generating a special quasi-random structure (SQS) of 8 f.u. (40 atoms) using

the Alloy Theoretic Automatic Toolkit (ATAT). As can be seen from the Fig. S4, the electronic density of states (DOS) of the SQS is similar to that we have obtained from 6 different La/Sr arrangements. Although the energy levels of oxygen vacancies are slight changed, the energy levels are still within the gap and the metal to semiconductor transition is still observed with two oxygen vacancies (δ=0.25). Thus, we have confirmed that the degree of disorder in the structure is not crucial to understand the effect of oxygen vacancies on electrical conductivity of $La_{0.5}Sr_{0.5}FeO_{3-\delta}$.

Electronic DOS for the 2x2x2 cubic supercell (8 f.u.) of $La_{0.5}Sr_{0.5}FeO_{3-\delta}$ (δ=0, 0.125, and 0.25) using the HSE06 method

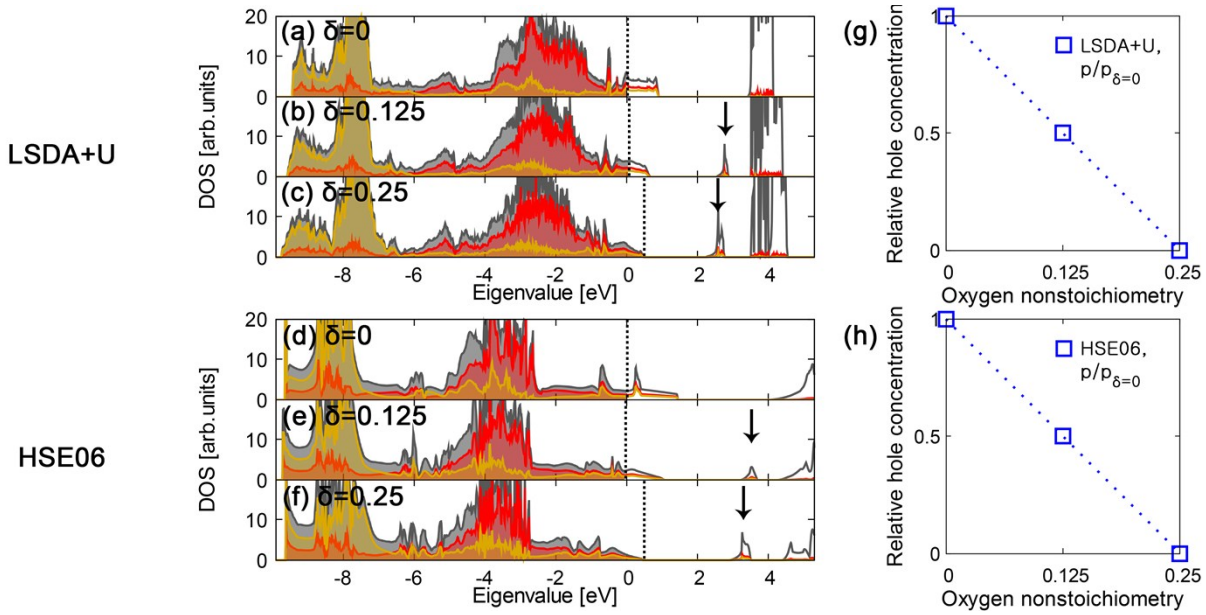

Figure. S5. Electronic DOS using LSDA+U calculations for (a) $La_{0.5}Sr_{0.5}FeO_3$, (b) $La_{0.5}Sr_{0.5}FeO_{2.875}$, and (c) $La_{0.5}Sr_{0.5}FeO_{2.750}$. Electronic DOS using HSE06 calculations for (d) $La_{0.5}Sr_{0.5}FeO_3$, (e) $La_{0.5}Sr_{0.5}FeO_{2.875}$, and (f) $La_{0.5}Sr_{0.5}FeO_{2.750}$. In (g) LSDA+U and (h) HSE06 calculations, relative hole concentration ($p/p_{\delta=0}$, blue square) as a function of oxygen nonstoichiometry, with value at stoichiometric state (δ=0) as a reference state. DOS of positive value indicates spin-up band. Black lines represent total DOS and Red (gold) lines show projected DOS for O (Fe). Filled (empty) regions represent occupied (unoccupied) states. Vertical dotted lines represent valence band maximum. Black arrows indicate oxygen vacancy states.

We have performed HSE06 calculations to verify our LSDA+U calculation results (see Fig. S5). Although bandgap has been slightly increased, the electronic density of states (DOS) obtained from the HSE calculations is similar to those obtained by the LSDA+U calculations; as oxygen vacancies increase, the holes in valence band are compensated by excess electrons from oxygen vacancies and finally the system turns to semiconducting phase with the vacancy concentration of δ=0.25. Thus, HSE results have successfully verified our LSDA+U calculation results.

V_O formation energy as a function of the Fermi energy

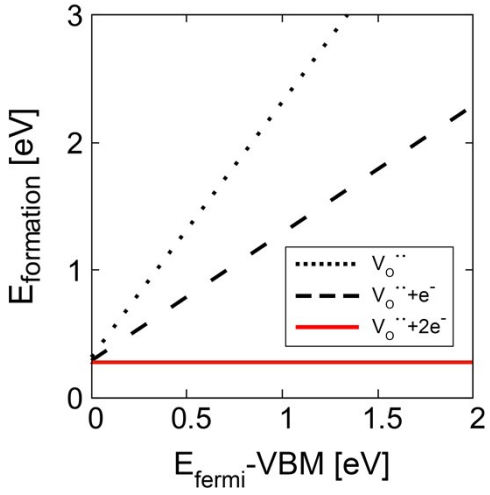

Figure. S6. Formation energy of oxygen vacancies with different excess electrons as a function of the Fermi energy. Since oxygen vacancy states are more unstable than the hybridized states, oxygen vacancies preferentially exist as V**Error!** (two positively charged state) by donating excess electrons to the system.

The V_O exist as charge state of +2 (V**Error!**) by donating electrons to the hybrid states, since the empty hybridized states are more stable than V**Error!** states. In other words, V**Error!**, V**Error!**, and neutral V_O preferentially exist as V**Error!**, V**Error!**+1e$^-$, and V**Error!**+2e$^-$, respectively. In addition, we calculated the defect formation energy (DFE) in order to understand energetically favorable number of excess electrons released from an oxygen vacancy. Fig. S6 shows the formation energy of charge state of V_O with different excess electrons as a function of the Fermi energy. As shown in the figure, the formation energy of V**Error!**+2e$^-$ is the most stable than others. Thus, an V_O preferentially provides 2 excess electrons into the system and becomes two positively charged.

The metal to semiconductor transition due to the excess electrons without oxygen vacancies

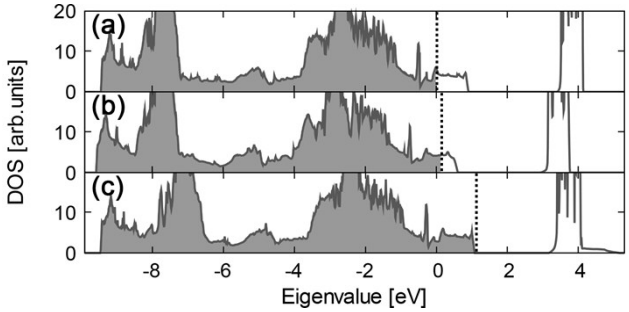

Figure. S7. Electronic density of states (DOS) for the 2n structure of (a) $La_{0.5}Sr_{0.5}FeO_3$, (b) $La_{0.5}Sr_{0.5}FeO_3$+2e$^-$, and (c) $La_{0.5}Sr_{0.5}FeO_{2.750}$+4e$^-$. Black lines represent total DOS. Filled (empty) regions represent occupied (unoccupied) states. Vertical dotted lines represent valence band maximum. Black arrows indicate oxygen vacancy states.

The hybridized band near the Fermi level is partially filled state at $La_{0.5}Sr_{0.5}FeO_3$ and $La_{0.5}Sr_{0.5}FeO_{2.875}$, and it becomes a fully occupied state at $La_{0.5}Sr_{0.5}FeO_{2.75}$. It seems like that excess electrons from the V_O shift the Fermi level and so change $La_{0.5}Sr_{0.5}FeO_{3-\delta}$ from the metallic to the semiconductor state. In order to verify that the metal to semiconductor transition is caused by excess electrons, we investigate the electric DOS for $La_{0.5}Sr_{0.5}FeO_3$ under excess electrons increase without an V_O. Fig. 7S(a-c) shows electric DOS for $La_{0.5}Sr_{0.5}FeO_{3-\delta}$ with different excess electrons (0e$^-$, 2e$^-$, and 4e$^-$), respectively. The Fermi level increases as excess electrons are introduced, and the hybridized band becomes fully occupied when 4e$^-$ are provided to system, as shown in the figure. Thus, the Fermi level shift and the metal to semiconductor transition under oxygen deficiency can be understood as the hole compensation by electrons released from V_O.

The effective masses along 7 different directions for 6 different structures of $La_{0.5}Sr_{0.5}FeO_{2.750}$

Table. S1. The effective masses of hole (m_h^*/m_0) along 7 directions (Γ-X, Γ-Y, Γ-Z, Γ-S, Γ-U, Γ-T, and Γ-R or Y-Γ, Y-X, Y-Z, Y-S, Y-U, Y-T, and Y-R) for 6 different structures of $La_{0.5}Sr_{0.5}FeO_{2.750}$: The effective masses of hole along a total of 42 directions. Minimum effective mass of hole is highlighted in bold.

6 different structures of $La_{0.5}Sr_{0.5}FeO_{2.750}$	Effective mass of hole (m_h^*/m_0)						
	Γ→X	Γ→Y	Γ→Z	Γ→S	Γ→U	Γ→T	Γ→R
The 1st La/Sr arrangement	0.0162	0.2266	0.0267	0.0296	0.0184	0.0358	0.0250
The 2nd La/Sr arrangement	**0.0144**	0.0634	0.0569	0.0228	0.0222	0.0391	0.0246
The 3rd La/Sr arrangement	0.0165	0.0960	0.0592	0.0261	0.0247	0.0387	0.0262
The 6th La/Sr arrangement	0.0186	0.2082	0.0568	0.0320	0.0238	0.0373	0.0262
	Y→Γ	Y→X	Y→Z	Y→S	Y→U	Y→T	Y→R
The 4th La/Sr arrangement	4.7450	0.0313	0.0325	0.0158	0.0242	0.0165	0.0162
The 5th La/Sr arrangement	3.3054	0.0322	0.0326	0.0165	0.0246	0.0166	0.0166

Table. S2. The effective masses of electron (m_e^*/m_0) along 7 directions (Γ-X, Γ-Y, Γ-Z, Γ-S, Γ-U, Γ-T, and Γ-R) for 6 different structures of $La_{0.5}Sr_{0.5}FeO_{2.750}$: The effective masses of electron along a total of 42 directions. Minimum effective mass of electron is highlighted in bold.

6 different structures of $La_{0.5}Sr_{0.5}FeO_{2.750}$	Effective mass of electron (m_e^*/m_0)						
	Γ→X	Γ→Y	Γ→Z	Γ→S	Γ→U	Γ→T	Γ→R
The 1st La/Sr arrangement	0.0222	0.0248	0.0208	0.0237	0.0216	0.0224	0.0227
The 2nd La/Sr arrangement	0.0220	0.0225	0.0223	0.0223	0.0224	0.0221	0.0223
The 3rd La/Sr arrangement	0.0288	0.0211	0.0212	0.0252	0.0242	0.0206	0.0238
The 4th La/Sr arrangement	0.0191	0.0241	**0.0179**	0.0214	0.0185	0.0207	0.0202
The 5th La/Sr arrangement	0.0205	0.0251	0.0183	0.0240	0.0193	0.0214	0.0219
The 6th La/Sr arrangement	0.0352	0.0221	0.0224	0.0242	0.0278	0.0209	0.0228

Reference list

1 P. E. Blöchl, *Phys. Rev. B*, 1994, **50**, 17953.
2 G. Kresse and J. Furthmüller, *Phys. Rev. B*, 1996, **54**, 11169-11186.
3 S. Dudarev, G. Botton, S. Savrasov, C. Humphreys and A. Sutton, *Phys. Rev. B*, 1998, **57**, 1505.
4 Z. Yang, Z. Huang, L. Ye and X. Xie, *Phys. Rev. B*, 1999, **60**, 15674.
5 I. Shein, K. Shein, V. Kozhevnikov and A. Ivanovskii, *Phys. Solid State*, 2005, **47**, 2082-2088.
6 A. M. Ritzmann, A. B. Muñoz-García, M. Pavone, J. A. Keith and E. A. Carter, *Chem. Mater.*, 2013, **25**, 3011-3019.
7 T. Das, J. D. Nicholas and Y. Qi, *J. Mater. Chem. A*, 2017, **5**, 25031-25043.
8 U. Shimony and J. M. Knudsen, *Phys. Rev.*, 1966, **144**, 361-366.
9 W. Koehler and E. Wollan, *J. Phys. Chem. Solids*, 1957, **2**, 100-106.
10 M. Reehuis, C. Ulrich, A. Maljuk, C. Niedermayer, B. Ouladdiaf, A. Hoser, T. Hofmann and B. Keimer, *Phys. Rev. B*, 2012, **85**, 184109.
11 R. H. Smit, Y. Noat, C. Untiedt, N. D. Lang, M. C. van Hemert and J. M. van Ruitenbeek, *Nature*, 2002, **419**, 906-909.
12 S. Wei, L. G. Ferreira, J. E. Bernard and A. Zunger, *Phys. Rev. B-Condens Matter*, 1990, **42**, 9622-9649.
13 A. Zunger, S. Wei, L. G. Ferreira and J. E. Bernard, *Phys. Rev. Lett.*, 1990, **65**, 353-356.
14 A. V. Krukau, O. A. Vydrov, A. F. Izmaylov and G. E. Scuseria, *J. Chem. Phys.*, 2006, **125**, 224106.
15 J. Heyd, G. E. Scuseria and M. Ernzerhof, *J. Chem. Phys.*, 2003, **118**, 8207-8215.
16 J. Heyd and G. E. Scuseria, *J. Chem. Phys.*, 2004, **121**, 1187-1192.
17 J. Heyd, G. E. Scuseria and M. Ernzerhof, *J. Chem. Phys.*, 2006, **124**.
18 A. van de Walle, P. Tiwary, M. de Jong, D. L. Olmsted, M. Asta, A. Dick, D. Shin, Y. Wang, L. Q. Chen and Z. K. Liu, *Calphad-Comput. Coupling Ph. Diagrams Thermochem.*, 2013, **42**, 13-18.